AGU ADVANCING EARTH AND SPACE SCIENCES

Earth and Space Science

RESEARCH ARTICLE
10.1029/2024EA003824

Can Large Strains Be Accommodated by Small Faults: "Brittle Flow of Rocks" Revised

Xiaoyu Zou[1] and Yuri Fialko[1]

[1]Institute of Geophysics and Planetary Physics, Scripps Institution of Oceanography, University of California San Diego, La Jolla, CA, USA

Key Points:

- We analyze the fault length-frequency distribution in developing (structurally immature) fault systems
- The cumulative frequency distribution follows a power law over a range of fault length spanning 8 orders of magnitude, with a negative exponent of ~2, consistent with the Gutenberg-Richter law
- Small faults within the brittle upper crust can accommodate a substantial (>30%) fraction of tectonic strain

Supporting Information:

Supporting Information may be found in the online version of this article.

Correspondence to:

X. Zou,
x3zou@ucsd.edu

Citation:

Zou, X., & Fialko, Y. (2024). Can large strains be accommodated by small faults: "Brittle flow of rocks" revised. *Earth and Space Science*, *11*, e2024EA003824. https://doi.org/10.1029/2024EA003824

Received 19 JUL 2024
Accepted 8 NOV 2024

Author Contributions:

Conceptualization: Yuri Fialko
Data curation: Xiaoyu Zou
Formal analysis: Xiaoyu Zou, Yuri Fialko
Funding acquisition: Yuri Fialko
Investigation: Xiaoyu Zou, Yuri Fialko
Methodology: Xiaoyu Zou, Yuri Fialko
Project administration: Yuri Fialko
Resources: Yuri Fialko
Software: Xiaoyu Zou, Yuri Fialko
Supervision: Yuri Fialko
Validation: Xiaoyu Zou, Yuri Fialko
Visualization: Xiaoyu Zou, Yuri Fialko
Writing – original draft: Xiaoyu Zou
Writing – review & editing: Xiaoyu Zou, Yuri Fialko

Abstract

Brittle deformation in the upper crust is thought to occur primarily via faulting. The fault length-frequency distribution determines how much deformation is accommodated by numerous small faults versus a few large ones. To evaluate the amount of deformation due to small faults, we analyze the fault length distribution using high-quality fault maps spanning a wide range of spatial scales from a laboratory sample to an outcrop to a tectonic domain. We find that the cumulative fault length distribution is well approximated by a power law with a negative exponent close to 2. This is in agreement with the earthquake magnitude-frequency distribution (the Gutenberg-Richter law with b-value of 1), at least for faults smaller than the thickness of the seismogenic zone. It follows that faulting is a self-similar process, and a substantial fraction of tectonic strain can be accommodated by faults that don't cut through the entire seismogenic zone, consistent with inferences of "hidden strain" from natural and laboratory observations. A continued accumulation of tectonic strain may eventually result in a transition from distributed fault networks to localized mature faults.

Plain Language Summary

The Earth's crust is pervasively damaged, and contains faults, fractures, and joints of various sizes and orientations. We use mapped fault traces from multiple data sets spanning a wide range of scales to investigate how much deformation is accommodated by small versus large faults. The fault length distribution is often assumed to be fractal, that is, following a power law. The power-law exponent α quantifies the relative contributions of many small faults relative to a few large ones. For $\alpha \leq 1$, the contribution of small faults is negligible, while for $\alpha \geq 2$, strains accommodated by small faults become significant. We find that the cumulative fault length distribution approximately follows a power law with an exponent $\alpha \geq 2$. This implies that small faults in developing shear zones can accommodate a substantial fraction of tectonic strain.

1. Introduction

Tectonic deformation in the upper crust is mainly accommodated by brittle failure, manifested in faults and tensile cracks (e.g., S. Cox & Scholz, 1988). Faults are ubiquitous in both intraplate settings and at plate boundaries (e.g., Woodcock, 1986; Bezerra et al., 2011; R. T. Cox et al., 2001; Twiss & Moores, 1992; Bürgmann & Pollard, 1994). As faults continue to slip, they increase their length via crack tip propagation, linkage, and coalescence (e.g., Mansfield & Cartwright, 2001; S. Cox & Scholz, 1988; Dawers & Anders, 1995; Fossen, 2020; Rotevatn et al., 2019). As a result, the upper crust contains faults of various sizes, from millimeter-long micro-fractures to mature faults extending hundreds of kilometers. The fault length distribution controls the relative contributions of small versus large faults to a total strain budget and is of interest to many disciplines including tectonics, engineering geology, hydrogeology, petroleum industry, and seismic hazards assessment (e.g., C. H. Scholz & Cowie, 1990; Bense et al., 2013; Bonnet et al., 2001; Kolawole et al., 2019).

Previous studies suggested a variety of functional forms describing the fault size distribution. It is generally believed that in a low-strain environment (e.g., developing shear zones), fault populations are fractal and thus follow a power-law distribution (e.g., Childs et al., 1990; D. Turcotte, 1986; Bour & Davy, 1999; Bonnet et al., 2001; Ben-Zion & Sammis, 2003). Nicol et al. (1996) noted that the fault length distribution may deviate from a power-law if a wide range of fault lengths is considered, and that the power-law exponent may vary at the low end of the fault length distribution owing to spatial clustering. In contrast, Odling et al. (1999) argued that the fault length distribution may appear as log-normal in individual data sets with a given detection threshold, but is a power-law for "composite" data sets that combine a number of individual data sets spanning a wide range of spatial scales. Other considered functional forms include gamma and exponential distributions that may provide a better fit to the data, especially at the distribution tails (e.g., Ackermann et al., 2001; Cowie et al., 1993; Michas et al., 2015; Spyropoulos et al., 1999). However, it is not always clear if departures from a power law are real, or due to sampling artifacts (e.g., Bonnet et al., 2001). Gupta and Scholz (2000) suggested a transition from a power-law to an exponential distribution when tectonic strain exceeds a critical threshold of the order of 0.1.

In case of a power-law distribution, the number of faults N that have lengths greater than or equal to L is given by

$$N(L) = CL^{-\alpha} \tag{1}$$

where C is an empirical constant, and $\alpha > 0$ is an absolute value of the power-law exponent, also known as the Pareto index (e.g., Clark et al., 1999). The derivative of the cumulative fault length distribution (Equation 1) with respect to L is the probability density,

$$\frac{dN}{dL} = C(1-\beta)L^{-\beta}, \tag{2}$$

which is also a power law, with $\beta = \alpha + 1$. The probability density (Equation 2) is sometimes referred to as the non-cumulative frequency distribution. A number of studies used field observations to test the assumption of a fractal distribution, and estimate parameters C and α (or β). Reported values of the best-fit power-law exponent α vary from 0.7 for faults in Chimney Rock, Utah (Cladouhos & Marrett, 1996; Krantz, 1988) to 1.1 for Neogene faults in the Boso and Iura Peninsula, Japan (C. H. Scholz & Cowie, 1990) to 2.3 for faults and fractures in sandstone in Tayma, Saudi Arabia (Odling et al., 1999). Most of the previous studies used data sets consisting of 10^2-10^3 fault traces with fault lengths spanning 1−2 decades.

The magnitude of the power-law exponent determines how deformation is partitioned between small and large faults. C. H. Scholz and Cowie (1990) estimated the power-law exponent $\alpha \approx 1$ using fault trace data from Japan and concluded that small faults are negligible in the total strain budget. In contrast, Kautz and Sclater (1988) argued, based on laboratory experiments and observations of natural faults, that small-scale faulting is responsible for a substantial internal deformation within crustal blocks bounded by major faults. Such deformation was also invoked to explain the relative rotation of conjugate faults in tectonically active regions such as the Eastern California Shear Zone (Fialko & Jin, 2021) and Tibet (Yin & Taylor, 2011). No such rotation would be possible if small faults were too scarce to accommodate a substantial fraction of tectonic strain.

To quantify the amount of deformation that can be attributed to small-scale faulting, we analyze the fault length distribution across a wide range of spatial scales using several high-quality data sets. In particular, we use detailed fault maps from different geological settings, including the Basin and Range Province (Nevada), Central Pennsylvania/Northern New Jersey, Ventura County (California), and Northern New Zealand. We complement these crustal-scale data sets with outcrop-scale observations of fractures and joints in Eastern Israel (Bahat, 1987) and Sierra Nevada (Segall & Pollard, 1983), and dip-slip faults in Southern New Zealand (Davis et al., 2005) and Eastern France (Villemin et al., 1995). We also use laboratory observations of Mode I and II micro-fractures in rock samples loaded to failure at confining pressures of several tens of megapascals (Katz & Reches, 2004). We examine the compiled multi-scale data to test the assumption of a power-law distribution, obtain the best-fit power-law exponent, and use the latter to estimate the amount of strain accommodated by faults in the upper crust, as a function of fault size.

2. Data and Methods

Continental deformation often involves broad regions of distributed faulting such as the Eastern California Shear Zone (Dokka & Travis, 1990; Floyd et al., 2020; Tymofyeyeva & Fialko, 2015), Basin and Range (Eaton, 1982; Hodges et al., 1989), and India-Arabia-Africa-Eurasia collision zone (e.g., England, 1987; Reilinger et al., 2006).

We are interested in the fault length-frequency distribution in regions of distributed deformation. Unfortunately, strike-slip faults are often difficult to recognize due to their limited geomorphologic expression, especially in case of small, low offset faults. Normal faults are better suited for this purpose because they produce scarps (changes in topography) that are easier to map. One of the most extensive and detailed fault trace data sets from an actively deforming extensional region is that from the Basin and Range (B&R) province in the Western US (Figure 1a). This region hosts a number of active Quaternary faults (e.g., Eaton, 1982; U.S. Geological Survey and Nevada

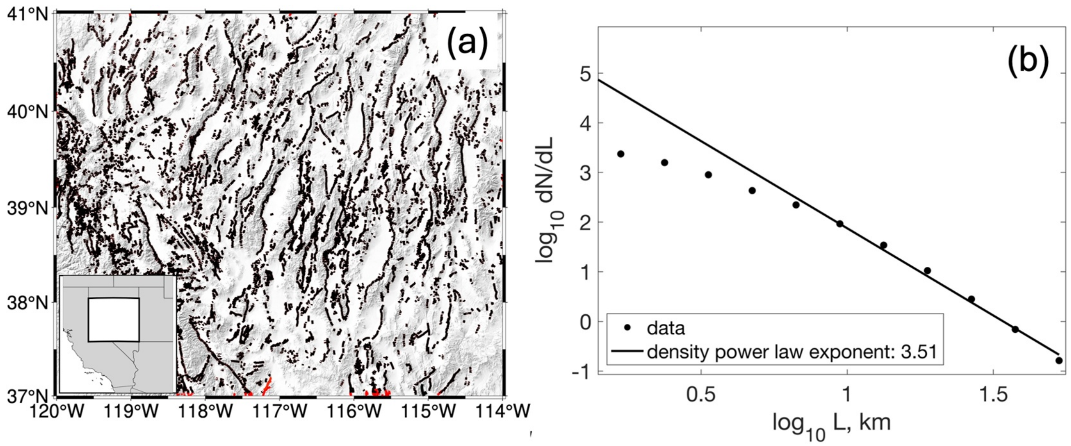

Figure 1. (a) Map of the Basin and Range Province (U.S. Geological Survey and Nevada Bureau of Mines and Geology, 2023). Shading denotes topography. Black lines denote fault traces. Red lines denote fault traces excluded from the analysis as they intersect the region boundaries. Inset shows location of the area of interest (white rectangle) in a regional context; thin black lines indicate state boundaries. The concatenated fault data set includes 10,825 fault segments. The minimum segment length is 2.1 m and the maximum length is 49 km. (b) Probability density of the fault length distribution, on a log-log scale. Solid line represents the best linear fit at the high end of the fault length distribution ($L > 5$ km). The estimated power-law exponent (slope of the best-fit line) is $\beta = 3.51 \pm 0.12$.

Bureau of Mines and Geology, 2023). We examine fault traces from an area extending 6° in longitude and 4° in latitude (Figure 1a). The respective data set consists of 26,512 fault traces, with the fault segment lengths varying from 2.1 m to 42.6 km.

A close inspection of the B&R fault trace data reveals that many fault traces that appear continuous on a regional scale (Figure 1a) are in fact highly segmented (Supplementary Figure S1a in Supporting Information S1). While some of the apparently continuous fault traces may be segmented because they have different attributes such as dip and strike, others may have the same attributes but are still separated at the segment level. To mitigate potential biases due to artificial segmentation, we developed an algorithm for concatenating individual segments that likely belong to the same fault. The algorithm attributes different segments to the same fault if the following criteria are satisfied: (a) tips of the adjacent fault segments are within a prescribed distance D from each other; (b) the adjacent fault segments are sufficiently well aligned, such that the difference in strike angles θ_1 and θ_2 between the segment tips (see Figure 2a) is less than a prescribed threshold δ; also, the difference between the average of strike angles at the segment tips, $(\theta_1 + \theta_2)/2$ and the strike angle of a line connecting the segment tips

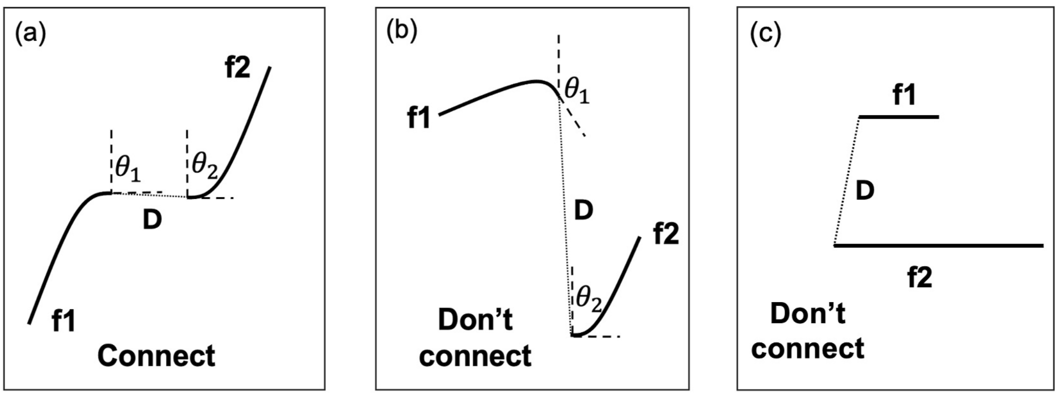

Figure 2. A schematic illustrating criteria used for connecting fault segments. Black solid lines denote fault traces (segments f1 and f2). D is the distance between fault tips. θ_1 and θ_2 are the local strike angles at the fault tips. The difference in strike angles is $\delta = |\theta_1 - \theta_2|$. (a) Segments f1 and f2 are allowed to be connected if the fault traces are sufficiently close and aligned (D and δ are below the prescribed thresholds). (b) Example of a configuration when the fault tips are not aligned (δ is larger than the prescribed threshold). (c) Example of a configuration of sub-parallel faults. In our analysis, we use $D \leq 5$ km and $\delta \leq 30°$.

is less than a prescribed threshold δ (Figure 2b); (c) overlapping segments that satisfy conditions (a) and (b) are considered part of the same fault if $D < L/3$, where L is the length of a smaller segment. The latter condition is meant to avoid absorption of small faults that are sub-parallel to (rather than aligned with) the large ones (Figure 2c). The respective criteria are illustrated in Figure 2.

A reasonable upper limit on D is some fraction of the thickness of the brittle layer T, such that the apparently discontinuous (e.g., poorly exposed) surface traces might possibly belong to the same fault at depth. For the Basin and Range province, $T \approx 15$ km (e.g., Pancha et al., 2006). We assume $D \leq 5$ km. This assumption is consistent with observations and models of earthquake ruptures jumping across nearby fault segments (e.g., Ando & Kaneko, 2018; Harris & Day, 1999; Jia et al., 2023). We find that the best-fit power-law exponent is relatively insensitive to the assumed value of D, for δ between 0 and 30° (Figures S2 and S3 in Supporting Information S1). Larger values of D and δ encourage segment linking, resulting in a smaller number of small faults, and consequently smaller absolute values of the best-fit power-law exponents. In our analysis, we use $D = 5$ km, and $\delta = 30°$ to provide a lower bound on α. A comparison of fault trace data before and after "de-segmentation" is shown in Figure S1 in Supporting Information S1.

Because the cumulative fault length distribution is known to be sensitive to finite size effects, which can bias determination of the exponent (e.g., Bonnet et al., 2001; Serafino et al., 2021), we use the density distribution (Equation 2) to estimate the power-law exponent β, unless indicated otherwise. The respective values of α are trivially given by $\alpha = \beta - 1$.

Figure 1b shows the probability density of fault length distribution for the "concatenated" Basin and Range data set (a subset is shown in Figure S1b in Supporting Information S1). To minimize the censoring bias (e.g., Torabi & Berg, 2011), we refine the data set by excluding faults that intersect the region boundaries (after the segment concatenation), see red lines in Figure 1a. On a log-log plot, the density distribution exhibits a quasi-linear trend for $L > 5$ km, and flattens out for smaller L. The roll-off at $L < 5$ km likely results from incomplete sampling (truncation bias, Torabi & Berg, 2011; Bonnet et al., 2001), analogous to saturation of the Gutenberg-Richter distribution below the magnitude of completeness (e.g., Woessner & Wiemer, 2005). The truncation bias may be due to a finite detection threshold and/or 2-D sampling of a 3-D fault population (e.g., Heifer & Bevan, 1990; Marrett & Allmendinger, 1991). We use the Kolmogorov-Smirnov (KS) test (Clauset et al., 2009) to identify the range of fault lengths $[L_{\min}, L_{\max}]$ that can be used for power-law fitting (see Supplementary Text S1 in Supporting Information S1 for details). We estimate the density power-law exponent β by the least squares linear regression over the interval $[L_{\min}, L_{\max}]$. The uncertainty on the best-fit slope is obtained by performing a regression for different bin sizes, and computing a standard deviation of the resulting slope estimates. For the data shown in Figure 1, we obtain $\beta = 3.51 \pm 0.12$, or $\alpha \approx 2.5$. This can be compared to the value of $\alpha = 1.84$ estimated by Cladouhos and Marrett (1996), who used an older (presumably, less complete) fault map of the Basin and Range province, and fitted a linear trend to the cumulative fault length distribution over the fault length interval between ~15–70 km.

We extended the same analysis to several other locations for which high-resolution maps of dip-slip faults are openly available, in particular, Central Pennsylvania and Northern New Jersey, Ventura County (California), and Northern New Zealand. Figure 3a shows fault traces from an area in Central Pennsylvania and Northern New Jersey (NJ Dept. of Environmental Protection Bureau of GIS, 2023; PA Department of Conservation & Natural Resources, 2023). The mapped traces represent inactive thrust and strike-slip faults formed 400 to 250 million years ago (Hatcher, 1987). For consistency, we apply the same algorithm for concatenating the aligned segments as described above. The resulting data set consists of 2,273 faults having length between 15 m and 108 km. The probability density fault length distribution (Figure 3b) is characterized by an apparent truncation for faults smaller than 20 km, and a slope of the quasi-linear trend of −3.51, remarkably similar to results obtained for the Basin and Range province (Figure 1b).

The Ventura County, CA (Figure 4) and Northern New Zealand (Figure 5) fault maps cover much smaller areas. After the segment concatenation procedure, each data set contains several hundreds of fault traces. This is 1–2 orders of magnitude smaller than the number of fault traces in the B&R and Pennsylvania/New Jersey data sets (Figures 1 and 3), but comparable to a typical size of data sets examined in a number of previous studies. While these smaller data sets are too characterized by decaying trends toward the high end of the sampled range of fault lengths, the data exhibit a significant scatter (e.g., Figure 5b), making power-law fits more problematic. Our

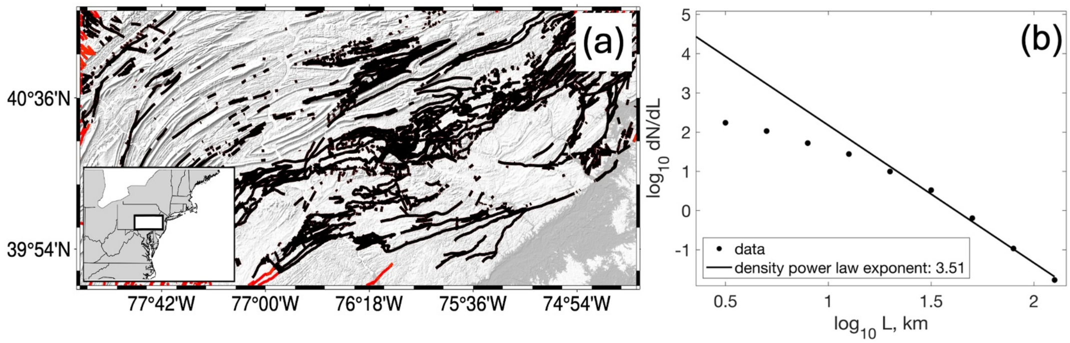

Figure 3. (a) Map of Central Pennsylvania and Northern New Jersey (NJ Dept. of Environmental Protection Bureau of GIS, 2023; PA Department of Conservation & Natural Resources, 2023). Notation is the same as in Figure 1. The concatenated fault data set includes 2,273 fault segments. The minimum segment length is 15 m and the maximum length is 108 km. (b) Probability density of the fault length distribution, on a log-log scale. Solid line represents the best linear fit at the high end of the fault length distribution ($L > 10$ km). The estimated power-law exponent (slope of the best-fit line) is $\beta = 3.51 \pm 0.20$.

analysis of the respective data sets yields smaller values of β that are subject to higher uncertainties (2.68 ± 0.14 for Ventura County and 2.42 ± 0.40 for Northern New Zealand, see Figures 4b and 5b).

To evaluate the fault length distribution at smaller scales, we use published data on fracture density measured in outcrops ($L \sim 1$–100 m) and laboratory samples ($L \sim 1$–100 mm). The outcrop-scale observations include reactivated joints in igneous rocks near Florance Lake, Sierra Nevada, California (Segall & Pollard, 1983) and Eocene chalks in the Syrian Arc folding belt, Israel (Bahat, 1987); thrust faults in the Ostler Fault Zone, Benmore outcrop, Southern New Zealand (Davis et al., 2005); and predominantly dip-slip faults in La Houve Coal Field, an old sedimentary basin in Eastern France that experienced both compressional and extensional tectonics (Villemin et al., 1995). The laboratory data are from specimens of Mount Scott granite of Oklahoma loaded to peak yield stress in a triaxial apparatus under confining pressure of 41 MPa (Katz & Reches, 2004). The micro-structural mapping of the sample damage was performed on scanned images of thin sections. Each sample had on the order of 10^3 resolved micro-fractures with lengths between 0.01 and 10 mm (Katz & Reches, 2004).

A compilation of the respective data sets is presented in Figure 6, along with the fault trace data from Figures 1 and 3–5. To enable a direct comparison of different data sets, we normalize the cumulative fault length counts by the areas from which the fault trace data were collected. The combined cumulative frequency distribution spans

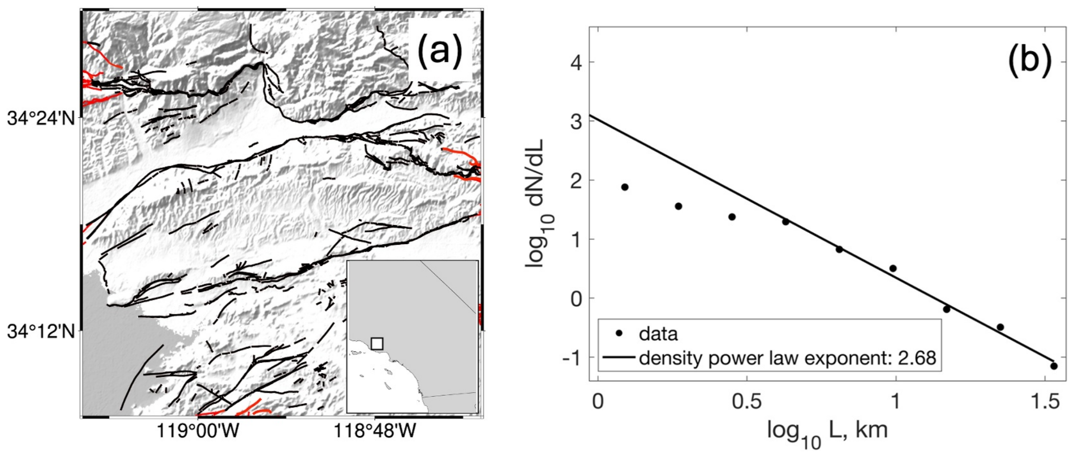

Figure 4. (a) Map of Ventura County, CA (County of Ventura, 2023). Notation is the same as in Figure 1. The concatenated fault data set includes 349 fault segments. The minimum segment length is 0.6 m and the maximum length is 30 km. (b) Probability density of the fault length distribution, on a log-log scale. Solid line represents the best linear fit at the high end of the fault length distribution ($L > 3$ km). The estimated power-law exponent (slope of the best-fit line) is $\beta = 2.68 \pm 0.14$.

10.1029/2024EA003824

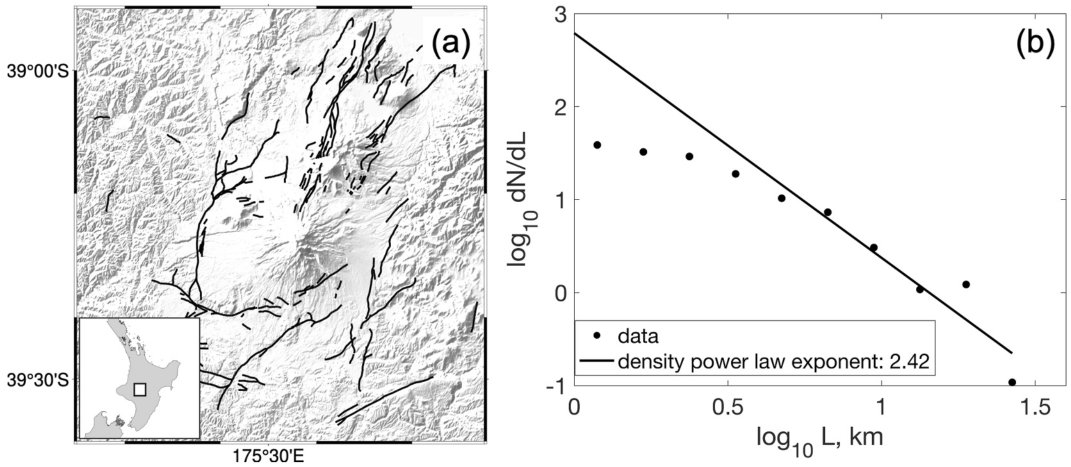

Figure 5. (a) Map of Northern New Zealand (Langridge et al., 2016a). Notation is the same as in Figure 1. The concatenated fault data set includes 159 fault segments. The minimum segment length is 363 m and the maximum length is 24.7 km. (b) Probability density of the fault length distribution, on a log-log scale. The solid line represents the best linear fit at the high end of the fault length distribution ($L > 4$ km). The estimated power-law exponent (slope of the best-fit line) is $\beta = 2.42 \pm 0.40$.

8 decades of fault length, and 18 decades of fault density (cumulative fault counts per unit area). All of the individual data sets shown in Figure 6 appear to have a log-normal distribution, with a quasi-linear trend at the high end, and a roll-off at the low end of the respective fault lengths. The high end quasi-linear trends have slopes that

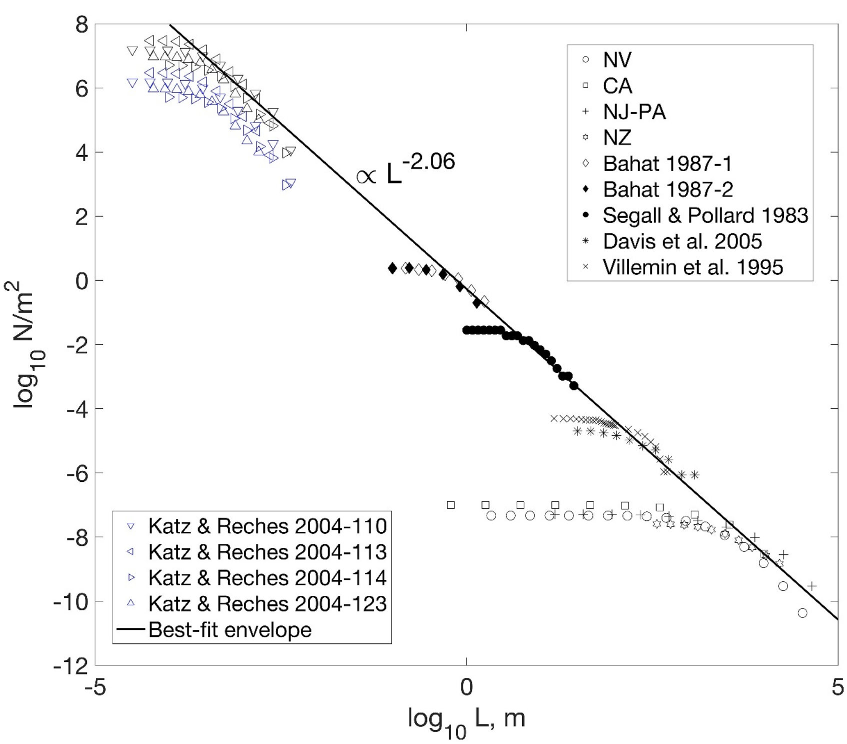

Figure 6. Cumulative fault length frequency distribution for a combined data set including fault traces (Figures 1–4), as well as outcrop-scale and lab data, normalized by the respective observation areas, on a log-log scale. The black solid line is the least squares fit to the "high-end" asymptotes of the outcrop- and crustal-scale data (black symbols, upper right legend). The estimated power-law exponent is $\alpha = 2.06$, and the pre-multiplying factor is $C = 0.53$. Blue triangles denote micro-crack length distributions from laboratory tests (Katz & Reches, 2004). Black triangles denote the same data shifted toward the best-fit envelope (black solid line).

are quite similar for all data sets shown in Figure 6, indicative of similar power-law exponents. Furthermore, the crustal- and outcrop-scale data admit a common envelope, suggesting that not only the power-law exponent, but also the multiplier C (Equation 1) is essentially the same across multiple data sets. The least squares fit of the common envelope to the crustal- and outcrop-scale data (see black solid line in Figure 6) yields a power-law exponent of $\alpha = 2.06$. The micro-crack data (blue triangles in Figure 6) parallel this trend, but fall somewhat below, suggesting a lower value of C (i.e., a smaller crack density). The least squares fit of an envelope to all of the data, including the micro-crack data (blue triangles in Figure 6), yields a power-law exponent of $\alpha = 1.93$ (not shown). To illustrate the overall similarity of the slope of the micro-crack length distribution to the rest of the data, we also plot the micro-crack data shifted toward the best-fit envelope ($\alpha = 2.06$, see black triangles in Figure 6).

3. Strain Due To Faults Obeying a Power Law Distribution

An overall agreement of the estimated power-law exponents of individual data sets between each other, on the one hand, and the common envelope, on the other hand (Figure 6), lends support to a suggestion that the roll-off in individual data sets is a result of truncation (e.g., due to a detection threshold, Bonnet et al., 2001; Torabi & Berg, 2011), and that the fault length statistics is adequately described by a power law across a wide range of spatial scales. If so, one can evaluate the amount of tectonic strain absorbed by faults of different sizes (e.g., C. H. Scholz & Cowie, 1990; J. Walsh et al., 1991).

For a population of n faults within the brittle crust having a volume TA, where T is the thickness of the brittle layer, and A is the map area, the average strain accommodated by faulting is given by (Kostrov, 1974):

$$\varepsilon_{ij} = \frac{1}{2TA}\sum_{k=1}^{n} {}^{k}P_{ij}. \tag{3}$$

In Equation 3, ${}^{k}P_{ij}$ is the seismic potency tensor (e.g., Ben-Zion, 2001) of the k-th fault in a population. The average fault slip S is expected to scale with fault length L,

$$S \propto L^{m}. \tag{4}$$

Theoretical arguments and field observations suggest that m should be close to one (e.g., Cowie & Scholz, 1992; Fialko, 2015), although higher values of m were suggested as well (e.g., J. J. Walsh & Watterson, 1988; Marrett & Allmendinger, 1991). Assuming $m = 1$,

$$S = \epsilon L, \tag{5}$$

where ϵ is the critical shear strain drop corresponding to fault propagation. The scalar potency is $P = \gamma SL^2$ for faults smaller than T, and $P = \gamma SLT$ otherwise, where γ is a geometric factor of the order of unity that accounts for the fault shape and fault dip (for faults that cut through the entire brittle layer, e.g., Vavra et al., 2023). For simplicity, hereafter we assume $\gamma = 1$. The number of faults within an interval of fault lengths ΔL is $(dN(L)/dL)\Delta L$. The cumulative potency can be calculated by integrating potencies of all faults for a given range of fault lengths. For faults smaller than T, the cumulative potency is (C. H. Scholz & Cowie, 1990):

$$p_1(L_{\min}, L_{\max}) = \sum_k {}^{k}P = -\epsilon\int_{L_{\min}}^{L_{\max}} \frac{dN(L)}{dL}L^3 dL = C\epsilon\frac{\alpha}{3-\alpha}L^{3-\alpha}\Big|_{L_{\min}}^{L_{\max}}, \tag{6}$$

where $L_{\min}$ and $L_{\max}$ are the minimum and maximum fault sizes, respectively. For faults that cut through the entire brittle layer ($L > T$),

$$p_2(L_{\min}, L_{\max}) = \sum_k {}^{k}P = -\epsilon T\int_{L_{\min}}^{L_{\max}} \frac{dN(L)}{dL}L^2 dL = C\epsilon T\frac{\alpha}{2-\alpha}L^{2-\alpha}\Big|_{L_{\min}}^{L_{\max}}. \tag{7}$$

We evaluate the relative contribution of faults smaller than a given size L to the total strain by allowing $L_{\min} \to 0$, and computing a ratio

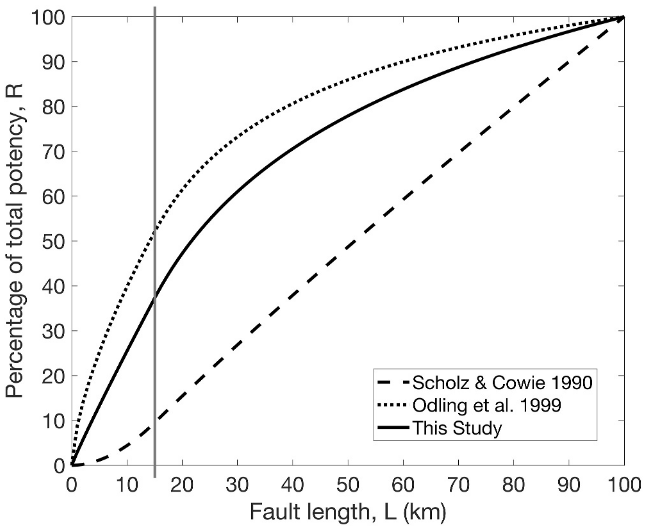

Figure 7. Percentage of the total potency R (Equation 8) accommodated by faults having length less than L, for several estimated values of the power-law exponent α: solid line, $\alpha = 2.06$ (this study); dotted line, $\alpha = 2.34$ (Odling et al., 1999); dashed line, $\alpha = 1.1$ (C. H. Scholz & Cowie, 1990). We assume $L_{\max} = 100$ km (Figure 6). The vertical gray line corresponds to $L = T = 15$ km.

$$R = 100\% \times \begin{cases} \dfrac{p_1(0,\, L)}{p_1(0,\, T) + p_2(T,\, L_{\max})}, & \text{for } L < T \\ \dfrac{p_1(0,\, T) + p_2(T,\, L)}{p_1(0,\, T) + p_2(T,\, L_{\max})}, & \text{for } L > T. \end{cases} \tag{8}$$

Note that R does not depend on factors C and ϵ. Figure 7 shows the percentage of strain accommodated by faults having length less than L, for a range of L, assuming $\alpha = 2.06$, $L_{\max} = 100$ km (Figure 6), and $T = 15$ km, typical of the seismogenic depth in many tectonically active areas (e.g., Pancha et al., 2006; E. O. Lindsey & Fialko, 2016; Jin et al., 2023; Jia et al., 2023). For a comparison, we also show analogous calculations for previously reported values of $\alpha = 1.1$ (dashed line, C. H. Scholz & Cowie, 1990) and $\alpha = 2.34$ (dotted line, Odling et al., 1999).

4. Discussion

For fault systems characterized by a power-law size distribution (1), the power-law exponent α controls how much of tectonic deformation is accommodated by numerous small faults versus a few large ones. C. H. Scholz and Cowie (1990) estimated the value of $\alpha = 1.1$ for a set of intraplate faults in Japan, and concluded that small faults are negligible in the overall strain budget. This is because integrals (6) and (7) are strongly convergent for $\alpha \approx 1$, so that the cumulative potency is dominated by the largest faults. Our results, based on a much larger data set, indicate $\alpha \geq 2$ (Figure 6). Most of the previously published estimates of α fall in the range between 1 and 2 (e.g., Bonnet et al., 2001). Possible reasons for different values of α reported in the literature include: (a) use of fault trace data of limited coverage and/or resolution; (b) uncertainties involved in defining fault connectivity; (c) a narrow range of fault lengths used in the analysis; (d) departures from self-similarity due to the presence of intrinsic length scales; (e) different stages of maturity of different fault systems. For example, the data set used by C. H. Scholz and Cowie (1990) spans only one order of magnitude of fault lengths, from ~10 to ~100 km, likely insufficient for a robust validation of a power-law distribution (Stumpf & Porter, 2012). C. Scholz et al. (1993) analyzed a data set from the Volcanic Tableland (California) with fault lengths spanning 2 orders of magnitude, from a few tens of meters to a few kilometers, and obtained a higher value of $\alpha \approx 1.3$. The latter under-predicts the slope at the upper tail of the fault length distribution of C. Scholz et al. (1993, their Figure 4), which the authors attributed to data censoring.

Our analysis of several high-resolution data sets (Figures 1, 3–6) suggests values of α close to 2, higher than those reported by C. H. Scholz and Cowie (1990) and C. Scholz et al. (1993), but consistent with results from other multi-resolution studies. In particular, Heifer and Bevan (1990) combined fault trace data with measurements of crack density in boreholes to infer $\alpha \approx 2$. Odling et al. (1999) performed a multi-scale analysis of the length distribution of faults and joints in sandstones in Saudi Arabia, and found the best-fit power-law exponent of 2.34 for a range of fault lengths spanning 4 orders of magnitude. Values of $\alpha \geq 2$ in sandstones may be due to strain-hardening deformation bands that may inhibit fault propagation and instead promote nucleation of numerous small faults. C. Scholz et al. (1993) cautioned against combining observations that include different fracture modes (e.g., faults and joints, Heifer & Bevan, 1990). However, it can be argued that the crack length distributions should not strongly depend on the fracture mode as mathematical expressions for stress fields due to shear and tensile cracks are essentially identical (e.g., Fialko, 2015), so that stress interactions within the crack network are expected to be similar (e.g., for shear and tensile cracks). This is consistent with results from previous studies. As noted by Bonnet et al. (2001), "…scaling exponents (notably, the length distribution exponent) are remarkably insensitive to the orientation of the slip vector, that is, whether or not fracturing is accompanied by shear (faults) or tensile (joints) displacement." Given that the total accommodated strain includes contributions from all types of fractures, it's not unreasonable to include fractures of different modes in the length-frequency analysis. Different data sets are expected to show some variability in the estimated power-law exponents given various lithologies, crustal layering, maturity states, and fault roughness, among other factors (e.g., Kim & Sanderson, 2005; Power et al., 1988). Nevertheless, an overall agreement between the estimated power-law exponents for different types

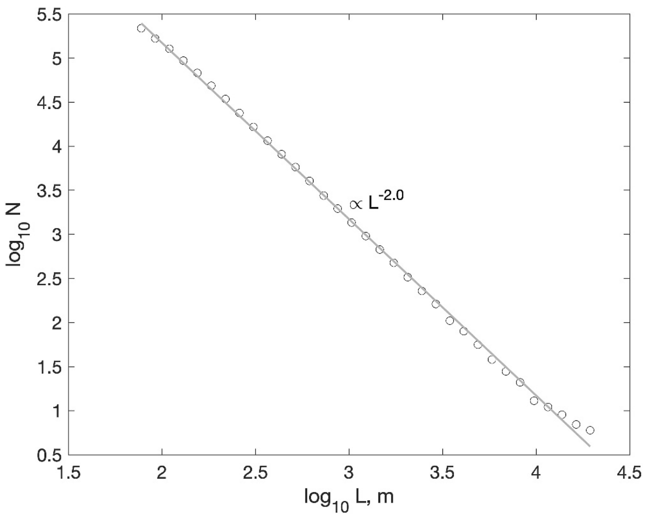

Figure 8. A cumulative fault length-frequency distribution of earthquakes that occurred in Southern California in 1981–2023. Open circles: earthquake data from the waveform-relocated catalog of Hauksson et al. (2012, updated annually), $1.7 \leq M \leq 6.5$. Solid gray line: best linear fit in log-log coordinates. Slope of the best-fit line is equal to -1.998.

of fractures, as well as for data sets from different locations (Figure 6) lends support to a hypothesis that early stages of faulting may be governed by a "universal" power law with $\alpha \approx 2$ (King, 1983; Proekt et al., 2012; Roman & Bertolotti, 2022).

The relative contribution of small faults to the strain budget is expected to be larger for smaller values of $L_{\max}$, and/or larger values of α. We note that the actual values of α may be in fact higher than those estimated from two-dimensional (2-D) sampling of three-dimensional (3-D) fault populations. For example, for uniformly distributed and randomly oriented faults, the true (i.e., 3-D) exponent is predicted to be larger than the exponent inferred from the 2-D sampling by as much as 1 unit (e.g., Bonnet et al., 2001; Marrett & Allmendinger, 1991). This only applies to small ($L < D$) faults, as for large faults the distribution is essentially 2-D. For α approaching 3, small faults would actually dominate the strain budget, and the contribution of large faults would be negligible. Note that for the cumulative potency and strain to remain finite, α cannot exceed 3 (Equation 6).

Some useful constraints on the fault length-frequency distribution can be obtained from the magnitude-frequency distribution of earthquakes. The latter obeys the well-established Gutenberg-Richter law, $\log_{10} N(M) = a - bM$, where $N(M)$ is the number of earthquakes with magnitude larger or equal to M, and a and b are empirical constants (Gutenberg & Richter, 1944). Unless otherwise noted, M denotes the moment magnitude, $M = \left(\log_{10} M_0 - 9.05\right)/1.5$, where M_0 is the scalar seismic moment (Hanks & Kanamori, 1979). Because M is related to a logarithm of M_0, it can be shown that parameter b (referred to as the "b-value") defines a power-law exponent α_s in the size-frequency distribution of seismic ruptures (e.g., King, 1983; D. L. Turcotte, 1997). In particular, the scalar seismic moment is given by $M_0 = \mu AS$, where μ is the shear modulus, A is the rupture area, and S is the average coseismic slip. For ruptures with moderate aspect ratios, $A \propto L^2$, and $S \propto L$, so that $M_0 \propto L^3$ (e.g., Fialko, 2015; Kanamori & Anderson, 1975). Substituting this scaling relation into expressions for the moment magnitude and magnitude-frequency distribution, one obtains $N(L) \propto L^{-2b}$, or $\alpha_s = 2b$. The coefficient of proportionality C can be found under additional assumptions, for example, by approximating earthquake ruptures as circular cracks with a constant stress drop $\Delta\sigma$. In this case, $A = \pi L^2/4$, and $S = 8\Delta\sigma L/7\pi\mu$ (e.g., Eshelby, 1957), leading to $L = (7M_0/2\Delta\sigma)^{1/3}$. Figure 8 shows a cumulative size-frequency distribution of earthquakes in Southern California recorded over the last 42 years since the deployment of digital seismic networks (Hauksson et al., 2012). The data set includes 7.7×10^5 earthquakes; shown in Figure 8 are events in the magnitude range from 1.7 (magnitude of completeness) to 6.5 (saturation of the seismogenic layer, $L \leq T$). To estimate rupture sizes from the moment magnitude, we choose a constant stress drop of 3 MPa (Abercrombie, 1995; Shearer et al., 2006). Note that the assumed value of $\Delta\sigma$ does not affect the power-law exponent α_s given stress drops do not systematically depend on L (Allmann & Shearer, 2009).

The earthquake data unambiguously indicate that seismically active faults within the seismogenic layer ($L < T$) have a power-law length-frequency distribution with an exponent α_s close to 2, corresponding to a b-value close to 1. The same b-value well describes the global seismicity, with some variations between 0.7 and 1.4 depending on the area and tectonic regime (Godano & Pingue, 2000; Schorlemmer et al., 2005; Shearer et al., 2006). For earthquakes that rupture the entire seismogenic zone ($M > 6.5$ for $T = 12 - 15$ km in most of the Western North America), the seismic moment no longer scales as a cube of L, leading to values of α_s that are smaller than $2b$. In particular, for $L > T$ the fault area is proportional to L, $A = LT$. The coseismic slip S is expected to saturate for $L > T$, but it appears to do so only for $L \gg T$ (e.g., Shaw & Scholz, 2001), giving rise to empirical scaling of S in proportion to either L (C. Scholz, 1994) or $\sqrt{L}$ (Leonard, 2010). Correspondingly, the seismic moment scales as either L^2 or $L^{3/2}$, yielding values of α_s of $4b/3$ or b. Assuming $b = 1$, this would suggest a change in the fault length-frequency distribution around $L \sim T$, with $\alpha_s \approx 2$ for "small" faults ($L < T$), and $\alpha_s \approx 1 - 1.3$ for "large" faults ($L > T$). However, it is unclear if b-value remains constant across the saturation length scale $L \sim T$. Regional data sets such as that shown in Figure 8 contain too few events with magnitudes greater than 6.5 to robustly evaluate the length-frequency distribution of earthquakes that rupture the entire seismogenic zone. To gain further insight, we use the global CMT catalog (Ekström et al., 2012) and examine the magnitude-frequency distribution of strike-slip earthquakes that occurred between 1976 and 2024 (see Figures S4 and S5 in Supporting Information S1). In the magnitude range between 5 and 6.5, the estimated b-value of the global data set is about 1 (Figure S4 in Supporting Information S1), consistent with the more complete Southern California data set spanning almost 5 units of earthquake magnitude, $1.7 \le M \le 6.5$ (Figure 8). However, strike-slip earthquakes that rupture the whole seismogenic zone, $6.5 \le M \le 8.1$, appear to have a larger b-value of ~1.3 (Figure S4 in Supporting Information S1). This gives rise to α_s of 1.3 (assuming $S \propto \sqrt{L}$) to 1.8 (assuming $S \propto L$) for "large" faults ($L > T$).

An excellent agreement between results shown in Figures 6 and 8 may be interpreted as indicating that the length-frequency distribution of seismically active faults is the same as that of the entire fault population, $\alpha_s \approx \alpha$. Alternatively, it can be argued that α_s is a lower bound on α, as only a fraction of faults within the seismogenic zone is seismically active (e.g., D. L. Turcotte, 1997, p. 44). This would be the case if estimates of α based on statistics of mapped fault traces suffer from a lower-dimensional bias (for $L < T$). The latter interpretation may be consistent with values of $\alpha > 2$ estimated from data sets that include large faults ($L > T$, Figures 1 and 3). Note that neither the fault length statistics of large ($L > T$) faults derived from the fault trace data, nor the values of α_s derived from the earthquake catalog data are subject to a lower-dimensional bias. In other words, α can be larger than 2 for the entire fault length distribution.

In any case, it is clear that values of $\alpha \sim 1$ reported in some previous studies are inconsistent with the Gutenberg-Richter statistics at the low end of the fault size distribution. For example, C. H. Scholz and Cowie (1990) suggested $\alpha = 1.1$ based on analysis of a data set dominated by large faults ($L \sim 10 - 100$ km). While this result might be reconciled with seismic observations in the limit $L > T$, it fails to describe the length-frequency distribution of small faults for which $\alpha \ge 2$ (Figure 6) as well as small-to-moderate earthquakes for which $\alpha_s \approx 2$ (Figure 8). In addition, our data sets that span the likely transition from "small" to "large" faults do not show obvious breaks in scaling and/or low values of α (Figures 1 and 3). However, the level of completeness of individual fault trace data sets is admittedly insufficient to make robust conclusions about potential variations in α across the presumed saturation length scale $L = T$.

We note that faults having lengths of tens to hundreds of kilometers have accumulated a substantial amount of slip, and thus may be more representative of a structurally mature fault system. Experimental studies reveal higher values of α at the initial stages of faulting when deformation is broadly distributed, and a decrease in α with an increasing system maturity (e.g., Cladouhos & Marrett, 1996; Hatton et al., 1993; Sornette et al., 1993). It follows that small faults can potentially accommodate a substantial fraction of tectonic strain at the initial stages of faulting (e.g., in developing shear zones). Over time, as faults grow and connect, deformation may localize to major faults that eventually take up most of the deformation.

These arguments suggest a distinction between deformation styles due to immature shear zones such as the Eastern California Shear Zone (Dokka & Travis, 1990; Floyd et al., 2020), and mature well-slipped plate boundary faults such as the San Andreas Fault (Fialko, 2006; Lisowski et al., 1991). In the latter case, interseismic strain accumulation is equal in magnitude, but opposite in sign to strain released in large earthquakes, so the patterns of interseismic and long-term (geologic) displacements across a mature fault are very different (Figure 9). A complete or nearly complete recovery of interseismic strain (i.e., elastic rebound) is evidenced by the good agreement between "geologic" and "geodetic" slip rates on major plate boundary faults (e.g., Schmalzle et al., 2006; Tatar et al., 2012; E. Lindsey & Fialko, 2013). In contrast, immature fault systems with $\alpha \ge 2$ give rise to a distributed inelastic deformation with the long-term displacement profile that may closely mimic the observed interseismic velocities (Fialko & Jin, 2021). The diffuse deformation pattern illustrated in Figure 9a can be thought of as resulting from the "seismic flow of rocks", as originally envisioned by Riznichenko (1965) and Kostrov (1974), although a more appropriate term would be the "brittle flow of rocks", since some of the deformation may occur aseismically, for example, via fault creep (Kaneko et al., 2013; Tymofyeyeva et al., 2019; Vavra et al., 2024). Additionally, some inelastic strain can result from other deformation mechanisms such as folding, bulk plasticity, pressure solution, etc (Donath & Parker, 1964; Hamiel et al., 2006; Hancock, 1985). The "brittle strain" estimated from the fault length-frequency statistics should thus be considered a lower bound on the total inelastic strain accommodated by the upper crust.

10.1029/2024EA003824

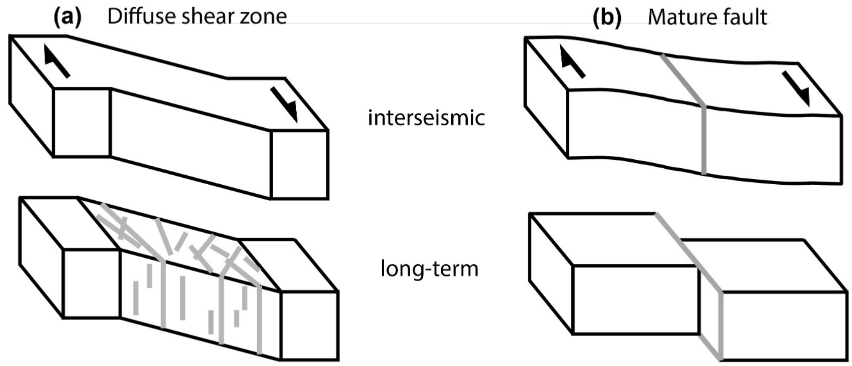

Figure 9. Schematic representation of kinematics of (a) developing shear zone and (b) mature plate boundary fault. Top and bottom panels denote interseismic and long-term (averaged over multiple earthquake cycles) motion, respectively. Gray lines denote active faults.

Taking at face value the estimated power law-exponent $\alpha \approx 2$ (Figure 6), we find that small ($L < T$) faults may take up more than one third of the total strain, which is much larger than predicted for $\alpha \approx 1$ (Figure 7). A power law-exponent $\alpha \geq 2$ may provide an explanation for the "missing strain" in palinspastic restorations of faults in sedimentary basins, as well as in laboratory models of tectonic extension using analog materials (e.g., Kautz & Sclater, 1988; Marrett & Allmendinger, 1992; J. Walsh et al., 1991). The bulk inelastic deformation accommodated by small faults can result in rotation of faults away from the optimal orientation, and increases in dihedral angles between conjugate faults, as often observed in active shear zones (e.g., Fialko, 2021; Ron et al., 2001; Zou et al., 2023). It might also account for the reported differences between geologic and geodetic slip rates in regions of diffuse deformation. In particular, models of deformation across the plate boundary in California suggest that up to 30% of deformation is accommodated off of the known faults (Field et al., 2014). Similar conclusions are drawn from numerical models of continental extension (Pan et al., 2023). Given no resolvable difference between the geologic and geodetic slip rates of mature high-slip-rate faults such as the San Andreas and San Jacinto faults (Segall, 2002; E. O. Lindsey et al., 2014; Tymofyeyeva & Fialko, 2018; Schmalzle et al., 2006), most of the "missing slip" is apparently associated with regions of diffuse deformation characterized by low strain rates such as the Eastern California Shear Zone (Herbert et al., 2014). The same may apply to other areas of broadly distributed continental deformation such as the India-Eurasia collision zone (e.g., Garthwaite et al., 2013; Wang & Shen, 2020; Yin & Taylor, 2011). A major outstanding question is how strongly the "true" power-law exponent α differs from estimates based on the fault trace data in case of small ($L < T$) faults, and/or "seismic" values of α_s based on the Gutenberg-Richter statistics. Values as high as 2.5 (or greater) would imply a diffuse long-term deformation similar to a viscous flow. Our results provide a lower bound on the amount of permanent strain accommodated in the upper crust off of major faults. Additional strain may be accommodated by other mechanisms such as pressure solution and bulk creep (e.g., Gratier et al., 2013; Hancock, 1985). Quantifying the respective contributions is a rich area for future research.

5. Conclusions

We analyzed the fault length frequency distribution using high-resolution fault trace data from diverse settings including Basin and Range Province, Central Pennsylvania/Northern New Jersey, Ventura County, California, and Northern New Zealand. To extend our analysis to smaller scales, we included published outcrop data from Sierra Nevada, Eastern Israel, Southern New Zealand, and Eastern France, and laboratory data from experiments on the initially intact granite samples. Our results indicate that while each individual data set yields an apparent log-normal distribution of fault lengths, a composite multi-scale data set reveals a fault length-distribution that follows a power law over 8 decades of fault lengths, with a cumulative power-law exponent $\alpha \approx 2$. This is consistent with the Gutenberg-Richter statistics of earthquakes with a typical b-value of 1. However, not all faults present in the seismogenic zone may be seismically active, and the obtained value of α may under-estimate the true value of the power-law exponent for example, due to an observation bias (2-D sampling of 3-D faults). We used the best-fit value of the power-law exponent to estimate the fraction of strain accommodated by faults as a function of fault size. We find that small faults ($L < 15$ km) can accommodate a substantial (more than 30%) fraction of tectonic strain, at least at the initial stages of faulting. This fraction may be substantially higher if the fault length statistics suffer from a low-dimensional bias, and the true value of α is between 2 and 3. A continued deformation may give rise to a transition from distributed fault networks to highly localized mature faults, associated with a decrease in α.

Conflict of Interest

The authors declare no conflicts of interest relevant to this study.

Data Availability Statement

The fault and fracture lengths data used in this paper, as well as the scripts used to perform the analysis are available at our Zenodo repository via https://doi.org/10.5281/ZENODO.13974204 (Zou & Fialko, 2024).

The original Nevada fault map data used for concatenation and lengths calculation is available at the US Quaternary Fault and Fold Database via https://www.usgs.gov/programs/earthquake-hazards/faults (U.S. Geological Survey and Nevada Bureau of Mines and Geology, 2023).

The original Ventura County fault map data used for concatenation and lengths calculation is available at the Ventura County Faults database via https://venturacountydatadownloads-vcitsgis.hub.arcgis.com/datasets/2e356ea3e3df4c0bbfb8cfd77681bf20_0/explore?location=34.423653%2C-119.059450%2C8.90 (County of Ventura, 2023).

The original Pennsylvania fault map data used for concatenation and lengths calculation is available at the PA Bedrock Geology Faults (Vector) database via https://newdata-dcnr.opendata.arcgis.com/datasets/DCNR::bedrock-geology-of-pennsylvania-faults-vector/about (PA Department of Conservation & Natural Resources, 2023).

The original New Jersey fault map data used for concatenation and lengths calculation is available at the Geologic Faults in New Jersey database via https://www.arcgis.com/home/item.html?id=3a5c8b0a00be4485bcd22281a76f8e23 (NJ Dept. of Environmental Protection Bureau of GIS, 2023).

The original New Zealand fault map data used for concatenation and lengths calculation is available at the New Zealand Active Faults Database: High Resolution via https://data.gns.cri.nz/af/ (Langridge et al., 2016b).

The Southern California earthquake catalog used for the analysis of the cumulative size-frequency distribution of earthquakes in Southern California recorded over the last 42 years is available at the 1981–2023 Catalog via scedc.caltech.edu/data/alt-2011-dd-hauksson-yang-shearer.html (Hauksson et al., 2024).

The global CMT catalog for the analysis of the magnitude-frequency distribution of strike-slip earthquakes that occurred between 1976 and 2024 is available at the Global CMT Catalog Search via www.globalcmt.org (Ekström et al., 2024).

Acknowledgments

We thank the Associate Editor David Baratoux, Nancye Dawers, John Naliboff, and three anonymous reviewers for comments and suggestions that improved this manuscript. This study was supported by NSF (EAR-1841273) and NASA (80NSSC22K0506). We thank Dr. Oded Katz for sharing the digitized microfracture data. Figures were produced using Generic Mapping Tools (GMT) (Wessel et al., 2013) and Matlab.

References

Abercrombie, R. (1995). Earthquake source scaling relationships from -1 to 5 M_{L} using seismograms recorded at 2.5-km depth. *Journal of Geophysical Research*, *100*(B12), 24015–24036. https://doi.org/10.1029/95jb02397

Ackermann, R. V., Schlische, R. W., & Withjack, M. O. (2001). The geometric and statistical evolution of normal fault systems: An experimental study of the effects of mechanical layer thickness on scaling laws. *Journal of Structural Geology*, *23*(11), 1803–1819. https://doi.org/10.1016/s0191-8141(01)00028-1

Allmann, B. P., & Shearer, P. M. (2009). Global variations of stress drop for moderate to large earthquakes. *Journal of Geophysical Research*, *114*(B1), B01310. https://doi.org/10.1029/2008jb005821

Ando, R., & Kaneko, Y. (2018). Dynamic rupture simulation reproduces spontaneous multifault rupture and arrest during the 2016 Mw 7.9 Kaikoura earthquake. *Geophysical Research Letters*, *45*(23), 12–875. https://doi.org/10.1029/2018gl080550

Bahat, D. (1987). Jointing and fracture interactions in middle Eocene chalks near beer Sheva, Israel. *Tectonophysics*, *136*(3), 299–321. https://doi.org/10.1016/0040-1951(87)90031-x

Bense, V., Gleeson, T., Loveless, S., Bour, O., & Scibek, J. (2013). Fault zone hydrogeology. *Earth-Science Reviews*, *127*, 171–192. https://doi.org/10.1016/j.earscirev.2013.09.008

Ben-Zion, Y. (2001). On quantification of the earthquake source. *Seismological Research Letters*, *72*(2), 151–152. https://doi.org/10.1785/gssrl.72.2.151

Ben-Zion, Y., & Sammis, C. G. (2003). Characterization of fault zones. *Pure and Applied Geophysics*, *160*(3), 677–715. https://doi.org/10.1007/978-3-0348-8010-7_11

Bezerra, F. H., do Nascimento, A. F., Ferreira, J. M., Nogueira, F. C., Fuck, R. A., Neves, B. B. B., & Sousa, M. O. (2011). Review of active faults in the Borborema province, intraplate South America—Integration of seismological and paleoseismological data. *Tectonophysics*, *510*(3–4), 269–290. https://doi.org/10.1016/j.tecto.2011.08.005

Bonnet, E., Bour, O., Odling, N. E., Davy, P., Main, I., Cowie, P., & Berkowitz, B. (2001). Scaling of fracture systems in geological media. *Reviews of Geophysics*, *39*(3), 347–383. https://doi.org/10.1029/1999rg000074

Bour, O., & Davy, P. (1999). Clustering and size distributions of fault patterns: Theory and measurements. *Geophysical Research Letters*, *26*(13), 2001–2004. https://doi.org/10.1029/1999gl900419

Bürgmann, R., & Pollard, D. D. (1994). Strain accommodation about strike-slip fault discontinuities in granitic rock under brittle-to-ductile conditions. *Journal of Structural Geology*, *16*(12), 1655–1674. https://doi.org/10.1016/0191-8141(94)90133-3

Childs, C., Walsh, J. J., & Watterson, J. (1990). A method for estimation of the density of fault displacements below the limits of seismic resolution in reservoir formations. In *North sea oil and gas reservoirs—ii* (pp. 309–318). Springer.

Cladouhos, T. T., & Marrett, R. (1996). Are fault growth and linkage models consistent with power-law distributions of fault lengths? *Journal of Structural Geology*, *18*(2–3), 281–293. https://doi.org/10.1016/s0191-8141(96)80050-2

Clark, R. M., Cox, S., & Laslett, G. M. (1999). Generalizations of power-law distributions applicable to sampled fault-trace lengths: Model choice, parameter estimation and caveats. *Geophysical Journal International*, *136*(2), 357–372. https://doi.org/10.1046/j.1365-246x.1999.00728.x

Clauset, A., Shalizi, C. R., & Newman, M. E. J. (2009). Power-law distributions in empirical data. *SIAM Review*, *51*(4), 661–703. https://doi.org/10.1137/070710111

County of Ventura. (2023). Ventura county gis data [dataset]. *faults*. Retrieved from https://venturacountydatadownloads-vcitsgis.hub.arcgis.com/datasets/2e356ea3e3df4c0bbfb8cfd77681bf20_0/explore?location=34.423653%2C-119.059450%2C8.90

Cowie, P. A., & Scholz, C. H. (1992). Physical explanation for the displacement-length relationship of faults using a post-yield fracture mechanics model. *Journal of Structural Geology*, *14*(10), 1133–1148. https://doi.org/10.1016/0191-8141(92)90065-5

Cowie, P. A., Vanneste, C., & Sornette, D. (1993). Statistical physics model for the spatiotemporal evolution of faults. *Journal of Geophysical Research*, *98*(B12), 21809–21821. https://doi.org/10.1029/93jb02223

Cox, R. T., Van Arsdale, R. B., Harris, J. B., & Larsen, D. (2001). Neotectonics of the southeastern Reelfoot rift zone margin, central United States, and implications for regional strain accommodation. *Geology*, *29*(5), 419–422. https://doi.org/10.1130/0091-7613(2001)029<0419:notsrr>2.0.co;2

Cox, S., & Scholz, C. (1988). On the formation and growth of faults: An experimental study. *Journal of Structural Geology*, *10*(4), 413–430. https://doi.org/10.1016/0191-8141(88)90019-3

Davis, K., Burbank, D. W., Fisher, D., Wallace, S., & Nobes, D. (2005). Thrust-fault growth and segment linkage in the active Ostler fault zone, New Zealand. *Journal of Structural Geology*, *27*(8), 1528–1546. https://doi.org/10.1016/j.jsg.2005.04.011

Dawers, N. H., & Anders, M. H. (1995). Displacement-length scaling and fault linkage. *Journal of Structural Geology*, *17*(5), 607–614. https://doi.org/10.1016/0191-8141(94)00091-d

Dokka, R. K., & Travis, C. J. (1990). Role of the Eastern California shear zone in accommodating Pacific-North American plate motion. *Geophysical Research Letters*, *17*(9), 1323–1327. https://doi.org/10.1029/gl017i009p01323

Donath, F. A., & Parker, R. B. (1964). Folds and folding. *Geological Society of America Bulletin*, *75*(1), 45–62. https://doi.org/10.1130/0016-7606(1964)75[45:faf]2.0.co;2

Eaton, G. P. (1982). The Basin and range province: Origin and tectonic significance. *Annual Review of Earth and Planetary Sciences*, *10*(1), 409–440. https://doi.org/10.1146/annurev.ea.10.050182.002205

Ekström, G., Nettles, M., & Dziewoński, A. (2012). The global CMT project 2004–2010: Centroid-moment tensors for 13,017 earthquakes. *Physics of the Earth and Planetary Interiors*, *200*, 1–9. https://doi.org/10.1016/j.pepi.2012.04.002

Ekström, G., Nettles, M., & Dziewoński, A. (2024). Global CMT web page [Dataset]. *CMT Catalog web search*. https://www.globalcmt.org/

England, P. C. (1987). Diffuse continental deformation: Length scales, rates and metamorphic evolution. *Philos. Trans. Roy. Soc. Ser. A*, *321*(1557), 3–22.

Eshelby, J. D. (1957). The determination of the elastic field of an ellipsiodal inclusion, and related problems. *Proceedings of the Royal Society of London A*, *241*(1226), 376–396.

Fialko, Y. (2006). Interseismic strain accumulation and the earthquake potential on the southern San Andreas fault system. *Nature*, *441*(7096), 968–971. https://doi.org/10.1038/nature04797

Fialko, Y. (2015). Fracture and frictional mechanics - theory. In G. Schubert (Ed.), *Treatise on geophysics* (2nd. ed., Vol. 4, pp. 73–91). Elsevier Ltd. https://doi.org/10.1016/b978-044452748-6.00062-6

Fialko, Y. (2021). Estimation of absolute stress in the hypocentral region of the 2019 Ridgecrest, California, earthquakes. *Journal of Geophysical Research*, *126*(7), e2021JB022000. https://doi.org/10.1029/2021jb022000

Fialko, Y., & Jin, Z. (2021). Simple shear origin of the cross-faults ruptured in the 2019 Ridgecrest earthquake sequence. *Nature Geoscience*, *14*(7), 513–518. https://doi.org/10.1038/s41561-021-00758-5

Field, E. H., Arrowsmith, R. J., Biasi, G. P., Bird, P., Dawson, T. E., Felzer, K. R., et al. (2014). Uniform California earthquake rupture forecast, version 3 (UCERF3) the time-independent model. *Bulletin of the Seismological Society of America*, *104*, 1122–1180. https://doi.org/10.1785/0120130164

Floyd, M., Funning, G., Fialko, Y. A., Terry, R. L., & Herring, T. (2020). Survey and continuous GNSS in the vicinity of the july 2019 ridgecrest earthquakes. *Seismological Research Letters*, *91*(4), 2047–2054. https://doi.org/10.1785/0220190324

Fossen, H. (2020). Chapter 8 - Fault classification, fault growth and displacement. In N. Scarselli, J. Adam, D. Chiarella, D. G. Roberts, & A. W. Bally (Eds.), *Regional geology and tectonics* (2nd ed., pp. 119–147). Elsevier.

Garthwaite, M. C., Wang, H., & Wright, T. J. (2013). Broadscale interseismic deformation and fault slip rates in the central Tibetan Plateau observed using InSAR. *Journal of Geophysical Research*, *118*(9), 5071–5083. https://doi.org/10.1002/jgrb.50348

Godano, C., & Pingue, F. (2000). Is the seismic moment–frequency relation universal? *Geophysical Journal International*, *142*(1), 193–198. https://doi.org/10.1046/j.1365-246x.2000.00149.x

Gratier, J.-P., Dysthe, D. K., & Renard, F. (2013). The role of pressure solution creep in the ductility of the Earth's upper crust. *Advances in Geophysics*, *54*, 47–179. https://doi.org/10.1016/b978-0-12-380940-7.00002-0

Gupta, A., & Scholz, C. H. (2000). Brittle strain regime transition in the Afar depression: Implications for fault growth and seafloor spreading. *Geology*, *28*(12), 1087–1090. https://doi.org/10.1130/0091-7613(2000)028<1087:bsrtit>2.3.co;2

Gutenberg, B., & Richter, C. F. (1944). Frequency of earthquakes in California. *Bulletin of the Seismological Society of America*, *34*(4), 185–188. https://doi.org/10.1785/bssa0340040185

Hamiel, Y., Katz, O., Lyakhovsky, V., Reches, Z., & Fialko, Y. (2006). Stable and unstable damage growth in rocks with implications to fracturing of granite. *Geophysical Journal International*, *167*(2), 1005–1016. https://doi.org/10.1111/j.1365-246x.2006.03126.x

Hancock, P. (1985). Brittle microtectonics: Principles and practice. *Journal of Structural Geology*, *7*(3), 437–457. https://doi.org/10.1016/0191-8141(85)90048-3

Hanks, T. C., & Kanamori, H. (1979). A moment magnitude scale. *Journal of Geophysical Research*, *84*(B5), 2348–2350. https://doi.org/10.1029/jb084ib05p02348

Harris, R. A., & Day, S. M. (1999). Dynamic 3d simulations of earthquakes on en echelon faults. *Geophysical Research Letters*, *26*(14), 2089–2092. https://doi.org/10.1029/1999gl900377

Hatcher, R. D. (1987). Tectonics of the southern and central appalachian internides. *Annual Review of Earth and Planetary Sciences*, *15*(1), 337–362. https://doi.org/10.1146/annurev.earth.15.1.337

Hatton, C., Main, I., & Meredith, P. (1993). A comparison of seismic and structural measurements of scaling exponents during tensile subcritical crack growth. *Journal of Structural Geology*, *15*(12), 1485–1495. https://doi.org/10.1016/0191-8141(93)90008-x

Hauksson, E., Yang, W., & Shearer, P. M. (2012). Waveform relocated earthquake catalog for Southern California (1981 to 2011). *Bulletin of the Seismological Society of America*, *102*(5), 2239–2244. https://doi.org/10.1785/0120120010

Hauksson, E., Yang, W., & Shearer, P. M. (2024). Waveform relocated earthquake catalog for Southern California [dataset]. *1981-2023 catalog*. https://scedc.caltech.edu/data/alt-2011-dd-hauksson-yang-shearer.html

Heifer, K., & Bevan, T. (1990). Scaling relationships in natural fractures-data, theory and applications. *Proc. eur. petrol. conf.*, *2*, 367–376.

Herbert, J. W., Cooke, M. L., Oskin, M., & Difo, O. (2014). How much can off-fault deformation contribute to the slip rate discrepancy within the eastern California shear zone? *Geology*, *42*(1), 71–75. https://doi.org/10.1130/g34738.1

Hodges, K. V., McKenna, L. W., Stock, J., Knapp, J., Page, L., Sternlof, K., et al. (1989). Evolution of extensional basins and basin and range topography west of Death Valley, California. *Tectonics*, *8*(3), 453–467. https://doi.org/10.1029/tc008i003p00453

Jia, Z., Jin, Z., Marchandon, M., Ulrich, T., Gabriel, A.-A., Fan, W., et al. (2023). The complex dynamics of the 2023 Kahramanmaraş, Turkey, M w 7.8-7.7 earthquake doublet. *Science*, *381*(6661), 985–990. https://doi.org/10.1126/science.adi0685

Jin, Z., Fialko, Y., Yang, H., & Li, Y. (2023). Transient deformation excited by the 2021 M7.4 Maduo (China) earthquake: Evidence of a deep shear zone. *Journal of Geophysical Research*, *128*(8), e2023JB026643. https://doi.org/10.1029/2023jb026643

Kanamori, H., & Anderson, D. L. (1975). Theoretical basis of some empirical relations in seismology. *Bulletin of the Seismological Society of America*, *65*, 1073–1095.

Kaneko, Y., Fialko, Y., Sandwell, D., Tong, X., & Furuya, M. (2013). Interseismic deformation and creep along the central section of the North Anatolian fault (Turkey): InSAR observations and implications for rate-and-state friction properties. *Journal of Geophysical Research*, *118*(1), 316–331. https://doi.org/10.1029/2012jb009661

Katz, O., & Reches, Z. (2004). Microfracturing, damage, and failure of brittle granites. *Journal of Geophysical Research*, *109*(B1). https://doi.org/10.1029/2002jb001961

Kautz, S. A., & Sclater, J. G. (1988). Internal deformation in clay models of extension by block faulting. *Tectonics*, *7*(4), 823–832. https://doi.org/10.1029/tc007i004p00823

Kim, Y.-S., & Sanderson, D. J. (2005). The relationship between displacement and length of faults: A review. *Earth-Science Reviews*, *68*(3), 317–334. https://doi.org/10.1016/j.earscirev.2004.06.003

King, G. C. P. (1983). The accomodation of large strains in the upper lithosphere of the earth and other solids by self-similar fault systems: The geometric origin of b-value. *Pure and Applied Geophysics*, *121*(5–6), 761–815. https://doi.org/10.1007/bf02590182

Kolawole, F., Johnston, C. S., Morgan, C. B., Chang, J. C., Marfurt, K. J., Lockner, D. A., et al. (2019). The susceptibility of Oklahoma's basement to seismic reactivation. *Nature Geoscience*, *12*(10), 839–844. https://doi.org/10.1038/s41561-019-0440-5

Kostrov, B. V. (1974). Seismic moment and energy of earthquakes and seismic flow of rock. *Izv., Acad. Sci., USSR, Phys. Solid Earth (Engl. Translation)*, *1*, 23–40.

Krantz, R. W. (1988). Multiple fault sets and three-dimensional strain: Theory and application. *Journal of Structural Geology*, *10*(3), 225–237. https://doi.org/10.1016/0191-8141(88)90056-9

Langridge, R., Ries, W., Litchfield, N., Villamor, P., Dissen, R. V., Barrell, D., et al. (2016a). The New Zealand active faults database. *New Zealand Journal of Geology and Geophysics*, *59*(1), 86–96. https://doi.org/10.1080/00288306.2015.1112818

Langridge, R., Ries, W., Litchfield, N., Villamor, P., Dissen, R. V., Barrell, D., et al. (2016b). The New Zealand active faults database [dataset]. *the nz active fault database: High-resolution*, *59*(1), 86–96. https://doi.org/10.1080/00288306.2015.1112818

Leonard, M. (2010). Earthquake fault scaling: Self-consistent relating of rupture length, width, average displacement, and moment release. *Bulletin of the Seismological Society of America*, *100*(5A), 1971–1988. https://doi.org/10.1785/0120090189

Lindsey, E., & Fialko, Y. (2013). Geodetic slip rates in the southern san Andreas Fault system: Effects of elastic heterogeneity and fault geometry. *Journal of Geophysical Research*, *118*(2), 689–697. https://doi.org/10.1029/2012jb009358

Lindsey, E. O., & Fialko, Y. (2016). Geodetic constraints on frictional properties and earthquake hazard in the Imperial Valley, Southern California. *Journal of Geophysical Research*, *121*(2), 1097–1113. https://doi.org/10.1002/2015jb012516

Lindsey, E. O., Sahakian, V. J., Fialko, Y., Bock, Y., Barbot, S., & Rockwell, T. K. (2014). Interseismic strain localization in the San Jacinto fault zone. *Pure and Applied Geophysics*, *171*(11), 2937–2954. https://doi.org/10.1007/s00024-013-0753-z

Lisowski, M., Savage, J., & Prescott, W. H. (1991). The velocity field along the San Andreas fault in central and southern California. *Journal of Geophysical Research*, *96*(B5), 8369–8389. https://doi.org/10.1029/91jb00199

Mansfield, C., & Cartwright, J. (2001). Fault growth by linkage: Observations and implications from analogue models. *Journal of Structural Geology*, *23*(5), 745–763. https://doi.org/10.1016/s0191-8141(00)00134-6

Marrett, R., & Allmendinger, R. W. (1991). Estimates of strain due to brittle faulting: Sampling of fault populations. *Journal of Structural Geology*, *13*(6), 735–738. https://doi.org/10.1016/0191-8141(91)90034-g

Marrett, R., & Allmendinger, R. W. (1992). Amount of extension on "small" faults: An example from the Viking graben. *Geology*, *20*(1), 47–50. https://doi.org/10.1130/0091-7613(1992)020<0047:aoeosf>2.3.co;2

Michas, G., Vallianatos, F., & Sammonds, P. (2015). Statistical mechanics and scaling of fault populations with increasing strain in the corinth rift. *Earth and Planetary Science Letters*, *431*, 150–163. https://doi.org/10.1016/j.epsl.2015.09.014

Nicol, A., Walsh, J., Watterson, J., & Gillespie, P. (1996). Fault size distributions — Are they really power-law? *Journal of Structural Geology*, *18*(2), 191–197. https://doi.org/10.1016/s0191-8141(96)80044-7

NJ Dept. of Environmental Protection Bureau of GIS. (2023). Geologic faults in New Jersey [dataset]. *faults*. Retrieved from https://www.arcgis.com/home/item.html?id=3a5c8b0a00be4485bcd22281a76f8e23

Odling, N., Gillespie, P., Bourgine, B., Castaing, C., Chiles, J., Christensen, N., et al. (1999). Variations in fracture system geometry and their implications for fluid flow in fractures hydrocarbon reservoirs. *Petroleum Geoscience*, *5*(4), 373–384. https://doi.org/10.1144/petgeo.5.4.373

PA Department of Conservation and Natural Resources. (2023). Pa bedrock geology [dataset]. *faults (vector)*. Retrieved from https://newdata-dcnr.opendata.arcgis.com/datasets/DCNR::bedrock-geology-of-pennsylvania-faults-vector/about

Pan, S., Naliboff, J., Bell, R., & Jackson, C. (2023). How do rift-related fault network distributions evolve? Quantitative comparisons between natural fault observations and 3D numerical models of continental extension. *Tectonics*, *42*(10), e2022TC007659. https://doi.org/10.1029/2022tc007659

Pancha, A., Anderson, J. G., & Kreemer, C. (2006). Comparison of seismic and geodetic scalar moment rates across the Basin and Range Province. *Bulletin of the Seismological Society of America*, *96*, 11–32.

Power, W. L., Tullis, T. E., & Weeks, J. D. (1988). Roughness and wear during brittle faulting. *Journal of Geophysical Research*, *93*(B12), 15268–15278. https://doi.org/10.1029/jb093ib12p15268

Proekt, A., Banavar, J. R., Maritan, A., & Pfaff, D. W. (2012). Scale invariance in the dynamics of spontaneous behavior. *Proceedings of the National Academy of Sciences*, *109*(26), 10564–10569. https://doi.org/10.1073/pnas.1206894109

Reilinger, R., McClusky, S., Vernant, P., Lawrence, S., Ergintav, S., Cakmak, R., et al. (2006). GPS constraints on continental deformation in the Africa-Arabia-Eurasia continental collision zone and implications for the dynamics of plate interactions. *Journal of Geophysical Research*, *111*(B5). https://doi.org/10.1029/2005jb004051

Riznichenko, Y. V. (1965). The flow of rocks as related to seismicity. *Doklady Akademii Nauk SSSR*, *161*(1), 96–98.

Roman, S., & Bertolotti, F. (2022). A master equation for power laws. *Royal Society Open Science*, *9*(12), 220531. https://doi.org/10.1098/rsos.220531

Ron, H., Beroza, G., & Nur, A. (2001). Simple model explains complex faulting. *Eos, Transactions American Geophysical Union*, *82*(10), 125–129. https://doi.org/10.1029/eo082i010p00125-01

Rotevatn, A., Jackson, C. A.-L., Tvedt, A. B., Bell, R. E., & Blækkan, I. (2019). How do normal faults grow? *Journal of Structural Geology*, *125*, 174–184. https://doi.org/10.1016/j.jsg.2018.08.005

Schmalzle, G., Dixon, T., Malservisi, R., & Govers, R. (2006). Strain accumulation across the Carrizo segment of the San Andreas Fault, California: Impact of laterally varying crustal properties. *Journal of Geophysical Research*, *111*(B5), B05403. https://doi.org/10.1029/2005jb003843

Scholz, C. (1994). A reappraisal of large earthquake scaling. *Bulletin of the Seismological Society of America*, *84*(1), 215–218.

Scholz, C., Dawers, N., Yu, J.-Z., Anders, M., & Cowie, P. (1993). Fault growth and fault scaling laws: Preliminary results. *Journal of Geophysical Research*, *98*(B12), 21951–21961. https://doi.org/10.1029/93jb01008

Scholz, C. H., & Cowie, P. A. (1990). Determination of total strain from faulting using slip measurements. *Nature*, *346*(6287), 837–839. https://doi.org/10.1038/346837a0

Schorlemmer, D., Wiemer, S., & Wyss, M. (2005). Variations in earthquake-size distribution across different stress regimes. *Nature*, *437*(7058), 539–542. https://doi.org/10.1038/nature04094

Segall, P. (2002). Integrating geologic and geodetic estimates of slip rate on the San Andreas fault system. *International Geology Review*, *44*(1), 62–82. https://doi.org/10.2747/0020-6814.44.1.62

Segall, P., & Pollard, D. D. (1983). Joint formation in granitic rock of the Sierra Nevada. *GSA Bulletin*, *94*(5), 563–575. https://doi.org/10.1130/0016-7606(1983)94<563:jfigro>2.0.co;2

Serafino, M., Cimini, G., Maritan, A., Rinaldo, A., Suweis, S., Banavar, J. R., & Caldarelli, G. (2021). True scale-free networks hidden by finite size effects. *Proceedings of the National Academy of Sciences*, *118*(2), e2013825118. https://doi.org/10.1073/pnas.2013825118

Shaw, B. E., & Scholz, C. H. (2001). Slip-length scaling in large earthquakes: Observations and theory and implications for earthquake physics. *Geophysical Research Letters*, *28*(15), 2995–2998. https://doi.org/10.1029/2000gl012762

Shearer, P. M., Prieto, G. A., & Hauksson, E. (2006). Comprehensive analysis of earthquake source spectra in southern California. *Journal of Geophysical Research*, *111*(B6). https://doi.org/10.1029/2005jb003979

Sornette, A., Davy, P., & Sornette, D. (1993). Fault growth in brittle-ductile experiments and the mechanics of continental collisions. *Journal of Geophysical Research*, *98*(B7), 12111–12139. https://doi.org/10.1029/92jb01740

Spyropoulos, C., Griffith, W. J., Scholz, C. H., & Shaw, B. E. (1999). Experimental evidence for different strain regimes of crack populations in a clay model. *Geophysical Research Letters*, *26*(8), 1081–1084. https://doi.org/10.1029/1999gl900175

Stumpf, M. P., & Porter, M. A. (2012). Critical truths about power laws. *Science*, *335*(6069), 665–666. https://doi.org/10.1126/science.1216142

Tatar, O., Poyraz, F., Gürsoy, H., Cakir, Z., Ergintav, S., & Akpınar, Z. (2012). Crustal deformation and kinematics of the eastern part of the North Anatolian Fault Zone (Turkey) from GPS measurements. *Tectonophysics*, *518*, 55–62.

Torabi, A., & Berg, S. S. (2011). Scaling of fault attributes: A review. *Marine and Petroleum Geology*, *28*(8), 1444–1460. https://doi.org/10.1016/j.marpetgeo.2011.04.003

Turcotte, D. (1986). A fractal model for crustal deformation. *Tectonophysics*, *132*(1), 261–269. https://doi.org/10.1016/0040-1951(86)90036-3

Turcotte, D. L. (1997). *Fractals and chaos in geology and geophysics* (2nd ed.). Cambridge University Press.

Twiss, R., & Moores, E. (1992). *Structural geology*. W.H. Freeman.

Tymofyeyeva, E., & Fialko, Y. (2015). Mitigation of atmospheric phase delays in InSAR data, with application to the Eastern California Shear Zone. *Journal of Geophysical Research*, *120*(8), 5952–5963. https://doi.org/10.1002/2015jb011886

Tymofyeyeva, E., & Fialko, Y. (2018). Geodetic evidence for a blind fault segment at the southern end of the san Jacinto Fault Zone. *Journal of Geophysical Research*, *123*(1), 878–891. https://doi.org/10.1002/2017jb014477

Tymofyeyeva, E., Fialko, Y., Jiang, J., Xu, X., Sandwell, D., Bilham, R., et al. (2019). Slow slip event on the southern San Andreas fault triggered by the 2017 M_{w}8.2 Chiapas (Mexico) earthquake. *Journal of Geophysical Research*, *124*(9), 9956–9975. https://doi.org/10.1029/2018jb016765

U.S. Geological Survey and Nevada Bureau of Mines and Geology. (2023). Quaternary fault and fold database for the United States [dataset]. *quaternary fault and fold database of the united states*. Retrieved from https://www.usgs.gov/programs/earthquake-hazards/faults

Vavra, E. J., Fialko, Y., Rockwell, T., Bilham, R., Štěpančíková, P., Stemberk, J., et al. (2024). Characteristic slow-slip events on the superstition hills fault, southern California. *Geophysical Research Letters*, *51*(12), e2023GL107244. https://doi.org/10.1029/2023gl107244

Vavra, E. J., Qiu, H., Chi, B., Share, P.-E., Allam, A., Morzfeld, M., et al. (2023). Active dipping interface of the Southern San Andreas fault revealed by space geodetic and seismic imaging. *Journal of Geophysical Research*, *128*(11), e2023JB026811. https://doi.org/10.1029/2023jb026811

Villemin, T., Angelier, J., & Sunwoo, C. (1995). Fractal distribution of fault length and offsets: Implications of brittle deformation evaluation—The Lorraine coal basin. In C. C. Barton & P. R. La Pointe (Eds.), *Fractals in the earth sciences* (pp. 205–226). Springer US.

Walsh, J., Watterson, J., & Yielding, G. (1991). The importance of small-scale faulting in regional extension. *Nature*, *351*(6325), 391–393. https://doi.org/10.1038/351391a0

Walsh, J. J., & Watterson, J. (1988). Analysis of the relationship between displacements and dimensions of faults. *Journal of Structural Geology*, *10*(3), 239–247. https://doi.org/10.1016/0191-8141(88)90057-0

10.1029/2024EA003824

Wang, M., & Shen, Z.-K. (2020). Present-day crustal deformation of continental China derived from GPS and its tectonic implications. *Journal of Geophysical Research*, *125*(2), e2019JB018774. https://doi.org/10.1029/2019jb018774

Wessel, P., Smith, W. H. F., Scharroo, R., Luis, J., & Wobbe, F. (2013). Generic mapping Tools: Improved version released. Eos, trans. *AGU*, *94*(45), 409–410. https://doi.org/10.1002/2013eo450001

Woessner, J., & Wiemer, S. (2005). Assessing the quality of earthquake catalogues: Estimating the magnitude of completeness and its uncertainty. *Bulletin of the Seismological Society of America*, *95*(2), 684–698.

Woodcock, N. H. (1986). The role of strike-slip fault systems at plate boundaries. *Philos. Trans. Roy. Soc. Ser. A*, *317*(1539), 13–29.

Yin, A., & Taylor, M. H. (2011). Mechanics of V-shaped conjugate strike-slip faults and the corresponding continuum mode of continental deformation. *GSA Bulletin*, *123*(9–10), 1798–1821. https://doi.org/10.1130/b30159.1

Zou, X., & Fialko, Y. (2024). Fault traces dataset for zou and fialko earth and space sciences manuscript [dataset]. *Zenodo*. https://doi.org/10.5281/ZENODO.13974204

Zou, X., Fialko, Y., Dennehy, A., Cloninger, A., & Semnani, S. J. (2023). High-angle active conjugate faults in the Anza-Borrego shear zone, southern California. *Geophysical Research Letters*, *50*(21), e2023GL105783. https://doi.org/10.1029/2023gl105783